Springer

Acta Mechanica Sinica

CrossMark click for updates

•RESEARCH PAPER•

Acta Mech. Sin., Vol. 38, 121466 (2022)
https://doi.org/10.1007/s10409-021-09011-x

Numerical studies on weak and strong ignition induced by reflected shock and boundary layer interaction

Chengyang Huang[1], Yuan Wang[2], Ralf Deiterding[3], Dehai Yu[1], and Zheng Chen[1*]

[1] *SKLTCS, CAPT, College of Engineering, Peking University, Beijing 100871, China;;*
[2] *Institute of Applied Physics and Computational Mathematics, Beijing 100094, China;;*
[3] *Aerodynamics and Flight Mechanics Research Group, University of Southampton, Highfield Campus, Southampton SO17 1BJ, UK*

Received September 18, 2021; accepted October 8, 2021; published online January 7, 2022

In shock tube experiments, the interaction between the reflected shock and boundary layer can induce shock bifurcation and weak ignition. The weak ignition can greatly affect the ignition delay time measurement in a shock tube experiment. In this work, two-dimensional simulations considering detailed chemistry and transport are conducted to investigate the shock bifurcation and non-uniform ignition behind a reflected shock. The objectives are to interpret the formation of shock bifurcation induced by the reflected shock and boundary layer interaction and to investigate the weak ignition and its transition to strong ignition for both hydrogen and dimethyl ether. It is found that the non-uniform reflection of the incident shock at the end wall produces a wedge-shaped oblique shock foot at the wall. The wedge-shaped structure results in strong interactions between reflected shock and boundary layer, which induces the shock bifurcation. It is demonstrated that the local high-temperature spots at the foot of the bifurcated shock is caused by viscous dissipation and pressure work. As the post-reflected shock temperature increases, the transition from weak ignition to strong ignition in a stoichiometric hydrogen/oxygen mixture is observed. The relative sensitivity of ignition delay time to the post-reflected shock temperature is introduced to characterize the appearance of weak ignition behind the reflected shock. Unlike in the hydrogen/oxygen mixture, weak ignition is not observed in the stoichiometric dimethyl-ether/oxygen mixture since it has a relatively longer ignition delay time and smaller relative sensitivity.

Shock tube, Weak ignition, Shock-boundary layer interaction

Citation: C. Huang, Y. Wang, R. Deiterding, D. Yu, and Z. Chen, Numerical studies on weak and strong ignition induced by reflected shock and boundary layer interaction, Acta Mech. Sin. **38**, 121466 (2022), https://doi.org/10.1007/s10409-021-09011-x

1. Introduction

The shock tube is widely used to study the ignition and detonation properties of different fuels [1-3]. The ignition delay time (IDT) measured in shock tube experiments is one of the main targets for kinetic model development and validation [3,4], and thereby shock tube plays a key role in chemical kinetics. In shock tube experiments, homogeneous ignition is expected to occur in the region between the reflected shock and the end wall. Unfortunately, in practice, non-uniform ignition might happen due to the non-uniform reflected-shock compression, shock attenuation, boundary layer growth, or the interaction between the reflected shock and boundary layer [5-8]. For example, the reflected shock and boundary layer interaction can result in shock bifurcation, which may induce local ignition and increase the error in IDT measurements [6,9-12]. In this study, the non-uniform ignition caused by the reflected shock and boundary layer interaction is investigated. The main background of this study is related to the ignition delay time measurement using the shock tubes rather than the ignition that occurs in the detonation engines or internal combustion engines.

The interaction between the reflected shock and boundary layer can cause shock bifurcation (e.g., Refs. [13-16]) as depicted in Fig. 1 [17]. The reflected shock propagates to the left after its collision with the end wall on the right side. A λ-shaped shock structure (see the blue lines in Fig. 1) is formed

*Corresponding author. E-mail address: cz@pku.edu.cn (Zheng Chen)
Executive Editor: Guowei He

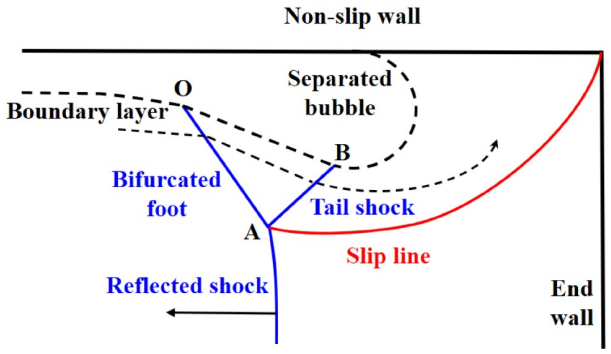

Figure 1 Schematic of the reflected shock and boundary layer interaction (adapted from Ref. [17]). Here A represents the triple point.

after the reflected shock and boundary layer interaction.

Due to the advantages of simulations, complex shock bifurcation has been studied numerically during the past decades. For example, Weber et al. [18] performed two-dimensional (2D) simulations of reflected shock and boundary layer interaction, and they examined the sensitivity of the interaction to the Reynolds number, the strength of incident shock and the heat transfer on the wall. Daru et al. [19,20] conducted high-resolution simulations for the shock bifurcation and found that the Reynolds number affects significantly the location of the triple point and the vortices produced within the lambda shock pattern. Based on the strength of the incident shock, Grogan and Ihme [21] examined three regimes for the reflected shock and boundary layer interaction, including incipient separation, shear layer instability and shock bifurcation. Recently, Chen et al. [22] have assessed the real gas effects on the vortex structure and triple point trajectory using a high-order point-implicit scheme. They found that the triple point trajectory is mainly affected by the shock strength rather than the chemical reaction.

The reflected shock and boundary layer interaction result in a non-uniform flow and temperature distribution behind the reflected shock. Such non-uniformity can induce the local autoignition and thereby affect the accuracy of IDT measurements in shock tube experiments [5,23]. Strehlow and Cohen [24] found that the reflected shock and boundary layer interaction can cause shock bifurcation and accelerate the reflected shock. The shock bifurcation changes the temperature distribution and induces local autoignition behind the reflected shock. Voevodsky and Soloukhin [25] identified two types of ignition, weak and strong ignition, behind the reflected shock in a stoichiometric hydrogen/oxygen mixture. They found that the boundary between the weak and strong ignition is located around the second explosion limit of hydrogen/oxygen. Meyer and Oppenheim [26] found that weak ignition is related to the sensitivity of ignition delay time, τ_{ig}, to the post-reflected shock temperature, T_5. They proposed a criterion ($\partial\tau_{ig}/\partial T_5 = -2$ μs/K) for the weak-to-strong ignition transition. This relationship was confirmed by other studies including the simulations. For example, Yamashita et al. [9] studied numerically and experimentally the ignition kernels appearing behind the reflected shock and proposed a criterion of the induction time gradient to distinguish the near-wall weak ignition from the far-wall strong ignition. Asahara et al. [27] reported that the detached vortices produced by the reflected shock and the boundary layer interaction are some of the key factors for local autoignition. Recently, Grogan and Ihme [6] have found that weak ignition is affected by the boundary conditions on the sidewall.

Most studies mentioned above have focused on the structure of fully developed shock bifurcation and the effects of weak ignition on IDT measurement. However, the transient development of the shock bifurcation and the afterward local ignition kernel is still not well understood. Besides, hydrogen was usually considered in previous numerical studies due to its compact chemical mechanism. There are few studies on other fuels and it is not clear whether weak ignition can be readily triggered by shock bifurcation for fuels other than hydrogen. Therefore, the objectives of this study are to simulate and interpret the formation of shock bifurcation induced by the interaction between the reflected shock and the boundary layer and to investigate the weak ignition and its transition to strong ignition for different fuels including both hydrogen and dimethyl ether. Two mixtures are considered here: one is stoichiometric hydrogen/oxygen (H_2/O_2) and the other is stoichiometric dimethyl-ether/oxygen (DME/O_2). Hydrogen is considered here since it is the simplest fuel with the most compact and well-developed chemical mechanism. DME is considered since it is one of the promising alternative fuels for engines. Besides, unlike hydrogen, DME has a negative temperature coefficient (NTC) with multi-stage ignition behavior, which is similar to most large hydrocarbon fuels used in engines. Besides, the chemical mechanism of DME is also relatively compact and well developed.

2. Numerical model and specifications

2D simulations considering detailed chemistry and transport are conducted to study the shock bifurcation and non-uniform ignition behind the reflected shock. The transient process is simulated using the parallel block-structured mesh refinement framework AMROC [28-31]. AMROC solves the fully compressible governing equations for 2D, multi-component, compressible flows using the second-order accurate MUSCL-Hancock finite volume method. A hybrid Roe-HLL Riemann solver, a conservative second-order accurate central difference scheme and the semi-implicit Runge-Kutta method GRK4A are used to solve the convective fluxes, multi-species diffusion terms and stiff reac-

tion terms, respectively. This efficient and adaptive solver has been extensively validated for ignition and detonation problems (e.g., Refs. [6,21,29-32]). The details on numerical methods, code validations, and grid convergence can be found in Refs. [28-34] and thereby are not repeated here.

Stoichiometric H_2/O_2 and DME/O_2 are considered here. The typical cases are listed in Table 1, in which the ignition delay time for 0D homogenous ignition and 2D reflected shocked induce ignition, sensitivity parameter and ignition mode shall be discussed in the next section. The detailed chemical mechanism for hydrogen (with 10 species and 21 elementary reactions) [35] is used in simulations. To reduce the computational cost, the skeletal chemical mechanism for DME with low-temperature chemistry (with 39 species and 175 elementary reactions) [36] is used. As shown in Ref. [36], the skeletal chemical mechanism for DME can accurately predict the multi-stage ignition and ignition delay time over a broad range of initial temperature and pressure.

Due to limitations in computational capability, we consider a small rectangular domain of $0 \le x \le 7$ or 12 cm and $0 \le y \le 0.8$ cm. The computational domain is large enough to ensure the boundary layer growth and its interaction with the reflected shock. The finest mesh size of 6.25 and 12.5 μm are used for H_2/O_2 and DME/O_2 mixtures, respectively. This ensures that there are at least 20 grid points per half-reaction length for the corresponding ZND structure. Grid convergence is ensured that the mesh resolution is sufficient to resolve the detailed structure of shock bifurcation and local ignition [37]. Besides, it has been shown [37] that the present simulation well captures the reflected shock and boundary layer interaction and λ-shaped shock structure measured by Damazo et al. [38].

The 2D computational domain is $0 \le x \le L_x$ and $0 \le y \le L_y$. Adiabatic, no-slip boundary conditions are used for the side wall located at $y = L_y = 0.8$ cm and for the end wall located at $x = L_x = 7$ or 12 cm. Symmetrical boundary conditions are enforced at $y = 0$ cm; and inlet boundary conditions are used at $x = 0$ cm. Initially there is an incident normal shock propagating in the x-direction towards the static H_2/O_2 or DME/O_2 mixture and it reflects on the end wall.

3. Results and discussion

3.1 Reflected shock and boundary layer interaction

In this subsection, we investigate the shock bifurcation caused by the reflected shock and boundary layer interaction in a stoichiometric H_2/O_2 mixture. The temperature and pressure after the reflected shock are 1068 K and 2.8 atm, respectively. The end wall is at $x = L_x = 7$ cm.

Figure 2 shows the temperature distribution near the boundary layer before the incident shock reflects on the right end wall. The fluid after the incident shock moves to the right side and a thin boundary layer develops on the side wall. Near the boundary, shock attenuation occurs and the shock becomes slightly curved as shown in Fig. 2. A detailed discussion on shock attenuation and shock curvature can be found in Refs. [22,39].

The transient evolution of the temperature contour during the shock reflection process is shown in Fig. 3. The timing starts (i.e., $t = 0$ μs) when the whole incident shock reflects and leaves the end wall. It is observed that at $t = -0.003$ μs, the main part of the incident shock reflects at the end wall for $y < 0.795$ cm, which results in a rapid increase of the temperature and pressure in region 5. However, due to its curved shape, part of the incident shock near the side wall with $y > 0.795$ cm still propagates toward the end wall. The pressure before the incident shock in region 1 is much lower than that

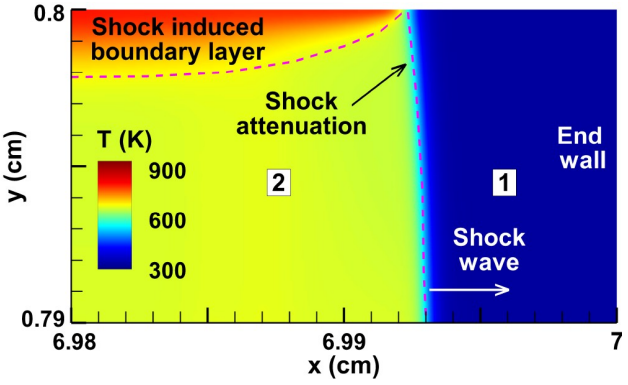

Figure 2 Temperature contour before the incident shock reflects on the right end wall. The mixture is stoichiometric H_2/O_2.

Table 1 Typical cases considered in this work

Mixture	States after reflected shock		Ignition delay time (μs)		Sensitivity parameter $\partial\tau_{ig}/\partial T_5$ (μs/K)	Ignition mode
	T_5 (K)	P_5 (atm)	0D	2D		
H_2/O_2	1068	2.85	61.1	41.5	5.54	Weak ignition
H_2/O_2	1073	2.85	48.2	40.2	3.53	Mixed mode of weak and strong ignition
H_2/O_2	1091	2.85	27.7	25.5	0.89	Strong ignition
H_2/O_2	1146	2.85	12.1	11.4	0.13	Strong ignition
DME/O_2	797	15	314.3	311.4	4.54	Strong ignition
DME/O_2	855	30	116.5	114.3	1.22	Strong ignition
DME/O_2	895	15	154.2	152.3	0.14	Strong ignition

in region 5. Consequently, such shock reflection results in a vertical pressure gradient, which drives the fluid to move toward the corner between the end wall and side wall. This was also observed by Chen et al. [22]. After the whole shock reflects on the end wall (i.e., $t > 0$ μs), the vertical pressure gradient still exists since the reflected shock closer to the boundary layer is relatively weaker due to the shock attenuation. Consequently, a wedge-shaped countercurrent flow structure forms as indicated by the streamlines in Fig. 4. In order to balance the pressure and velocity on both sides of the reflected shock, the wedge-shaped structure gradually evolves into a wedge-shaped oblique shock, which flattens the curved reflected shock front. Such kind of structure evolution was observed before by Davies and Wilson [15].

During the propagation of the reflected shock, the stagnation pressure inside the boundary layer is smaller than that behind the reflected shock. The fluid in the boundary layer fails to smoothly penetrate into the reflected shock region. Then the boundary layer separates from the wall as shown in Fig. 5. The fluid accumulates around the foot of the bifurcated shock, which results in a reversed flow and separation bubble. The size of the bifurcated shock structure and the separation bubble grows during the reflected shock propagation. In order to match the pressure difference behind the oblique shock AO and the normal reflected shock AC, another oblique shock AB develops. Consequently, the λ-shaped shock structure appears as shown in Fig. 5. Starting from triple point A, there is a slip line (indicated by the negative vorticity in Fig. 5) separating the flow compressed by the normal reflected shock AC from that by the oblique shocks AO and AB.

The above shock bifurcation inevitably induces a local temperature rise in the flow behind the reflected shock. When the IDT of the H_2/O_2 mixture after the reflected shock is much longer than the duration of the reflected shock propagation, the heat release due to chemical reactions is negligible. Therefore, the local temperature rise can only be caused by the work of pressure and viscous dissipation. To interpret the local temperature rise, we plot in Fig. 6a the contour of temperature, the absolute value of pressure work and viscous dissipation immediately after the shock reflection (i.e., the reflected shock is very close to the end wall). Figure 6 shows that the temperature after two oblique shocks is smaller than that after the normally reflected shock. This is because the normally reflected shock is much stronger than the oblique shocks. The adverse pressure gradient near the shock bifurcation leads to a reversed flow and the separation of the boundary layer. This results in a large velocity gradient and strong viscous dissipation near the side wall as shown in Fig. 6a. Near the side wall (region III in Fig. 6a), the pressure

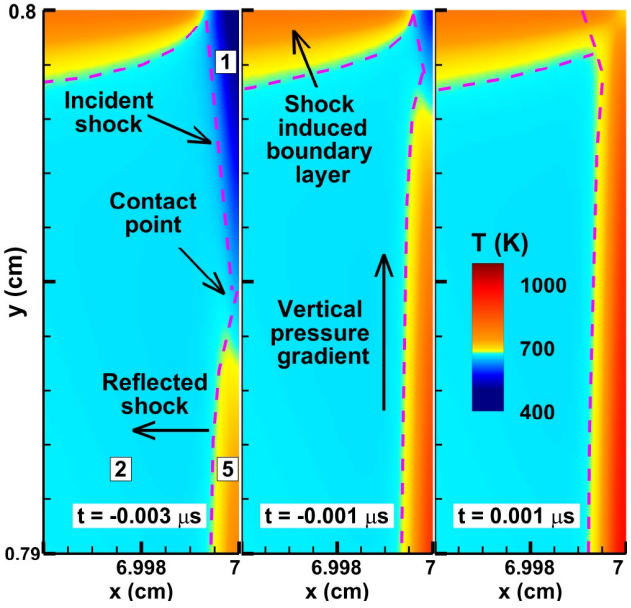

Figure 3 Evolution of the temperature contour during the shock reflection process on the end wall. The mixture is stoichiometric H_2/O_2, and T_5 = 1068 K and P_5 = 2.8 atm.

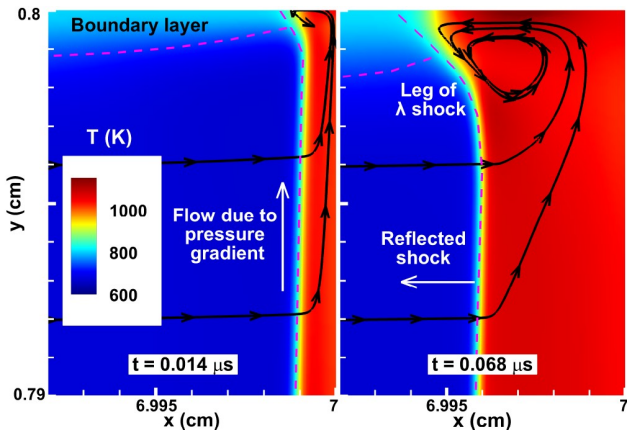

Figure 4 Evolution of the temperature contour and streamlines in the wedge-shaped oblique shock structure near the boundary layer. The mixture is stoichiometric H_2/O_2, and T_5 = 1068 K and P_5 = 2.8 atm.

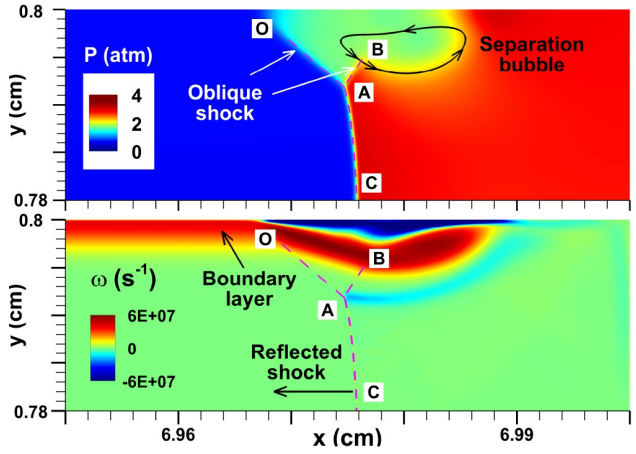

Figure 5 Pressure and vorticity counter at t = 0.418 μs. The dashed line AC represents the normal reflected shock; and the dashed lines AO and AB are two oblique shocks. The mixture is stoichiometric H_2/O_2, and T_5 = 1068 K and P_5 = 2.8 atm.

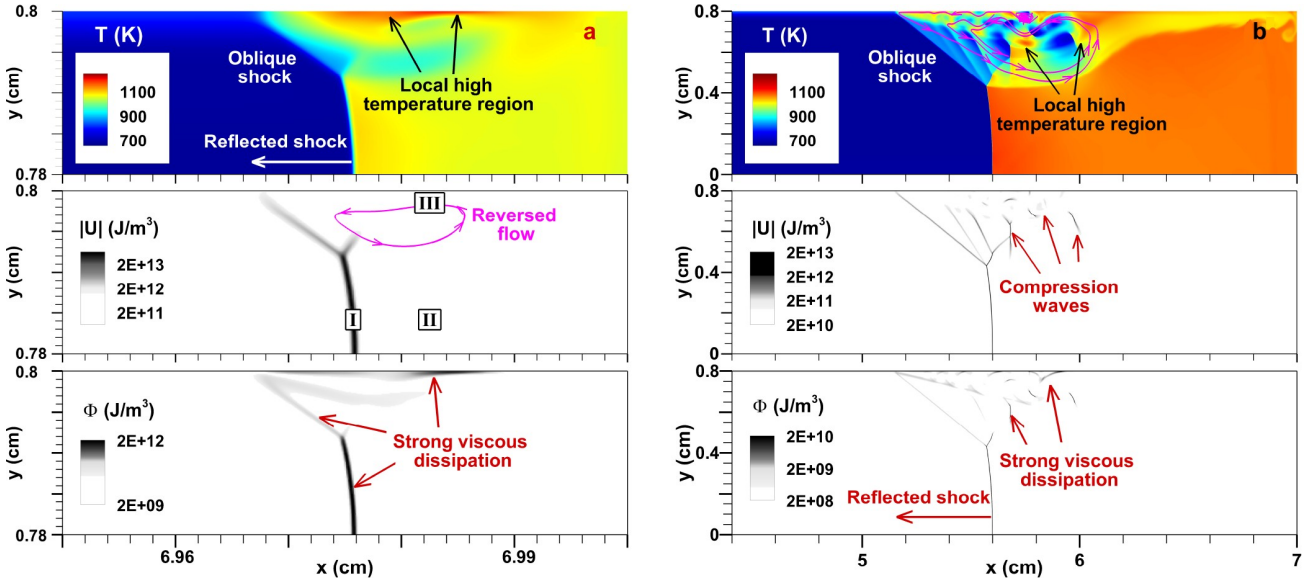

Figure 6 Contour of temperature: T, absolute value of pressure work: $|U|$, and viscous dissipation: Φ, after shock reflection: **a** t = 0.418 μs when the reflected shock is very close to the end wall, and **b** t = 23.5 μs when the reflected shock is some distance away from the end wall. The mixture is stoichiometric H_2/O_2, and T_5 = 1068 K and P_5 = 2.8 atm.

work is much smaller than the viscous dissipation. Therefore, it is the viscous dissipation that results in the local temperature rise near the side wall. This is consistent with previous results of Ziegler [32] and Grogan and Ihme [6]. Figure 6a shows that both pressure work and viscous dissipation are very large around the reflected shock (region I). Nevertheless, this only globally increases the temperature in region II and does not induce local temperature rise.

The results for the reflected shock being around 1.4 cm away from the end wall are shown in Fig. 6b. During the reflected shock propagation, the shock bifurcation gradually grows and more complex flow and shock structure are observed in Fig. 6b than in Fig. 6a. Due to the relative weakness of the oblique shock near the boundary layer, cold fluid before the shocks can be transported to the region after the oblique shocks, resulting in the so-called cold gas contamination [15,16]. Consequently, some relatively cold regions appear after the oblique shocks as shown in Fig. 6b. Figure 6b indicates that the viscous dissipation is a few orders smaller than the pressure work in the bifurcated region. This is because there are pressure waves produced due to the complex flow and shock interaction. These compression waves collide with one another or with the oblique shocks, resulting in the local temperature rise. The detached vortexes from the boundary layer transport the mixtures heated by pressure work downstream. Consequently, several ignition kernels with relatively high-temperature form around the foot of the bifurcated shock, which induces local weak ignition to be discussed in the next subsection.

In a brief summary, the above results demonstrate that the viscous dissipation and pressure work are the main causes for local temperature rise around the bifurcated shock. The viscous dissipation dominates at the very beginning after the shock reflection, while the pressure work gradually dominates during the subsequent evolution.

3.2 Weak ignition and its transition to strong ignition

In this subsection, we study the weak ignition and its transition to strong ignition as the post-reflected shock temperature increases. The post-reflected shock pressure is fixed to be P_5 = 2.8 atm. The stoichiometric H_2/O_2 mixture is considered and the end wall is at x = 7 cm.

For a relatively low post-reflected shock temperature of T_5 = 1068 K, the transient evolution of temperature distribution is shown in Fig. 7.

At t = 34.7 μs, several regions with local high temperature are shown to appear at the foot of bifurcated shock due to the viscous dissipation and pressure work discussed in the previous subsection. The local high temperature triggers chemical reactions in the H_2/O_2 mixture and induces local ignition in the stagnation region of bifurcated shock around t = 41.5 μs. Ignition first occurs at some distance away from the reflecting end wall. This is the so-called "weak ignition" phenomenon [25]. The ignition kernel expands and the local heat release produces pressure waves which compress the unburned mixture. Consequently, several ignition kernels are induced at the central region around t = 49.9 μs. Finally, the whole mixture behind the reflected shock ignites. Therefore, the local ignition is mainly induced by the reflected shock and boundary layer interaction under this relatively low post-reflected shock temperature. The instabilities in the shear layer are very strong, which will induce many strong vortical structures, and create many chaotic shocklets behind the

oblique shock.

Then we increase the post-reflected shock temperature to T_5 = 1073 K while keeping the pressure to be around P_5 = 2.8 atm. The results are shown in Fig. 8.

Figure 8 shows that the local high temperature appears not only in the stagnation region of bifurcated shock but also around the slip line close to the end wall. The slip line represents a thin vorticity layer, which is extremely unstable during the shock bifurcation and it curls and rolls up [9,18,27,40,41]. A vortex circle is observed near the corner between the end wall and side wall, which has relatively high temperature and reactivity. Since the mixture around the corner is first compressed by the reflected shock, it ignites earlier than the surrounding mixture. Consequently, two ignition kernels, one at the foot of bifurcated shock and the other close to the end wall, simultaneously appear at t = 40.2 μs, as shown in Fig. 8. These two ignition kernels propagate outwardly and produce pressure waves that compress the unburned mixture. Finally, a detonation develops near the end wall due to the coherent coupling between ignition and pressure wave, which can be explained by the SWACER (Shock Wave Amplification by Coherent Energy Release) mechanism [6,42,43]. During this ignition process, both weak ignition at the foot of bifurcated shock and strong ignition near the end wall happen. Therefore, it is a transition from pure weak ignition to pure strong ignition. The local ignition behaviors are mainly induced by the reflected shock and boundary layer interaction and the non-uniformities of flow near the end wall. To the authors' knowledge, such a mixed-mode of weak and strong ignition was not reported in previous studies including the work of Grogan and Ihme [6].

When the post-reflected shock temperature is further increased to T_5 = 1091 K, transition to strong ignition is observed as shown in Fig. 9. The higher post-reflected shock temperature results in a shorter ignition delay time for the

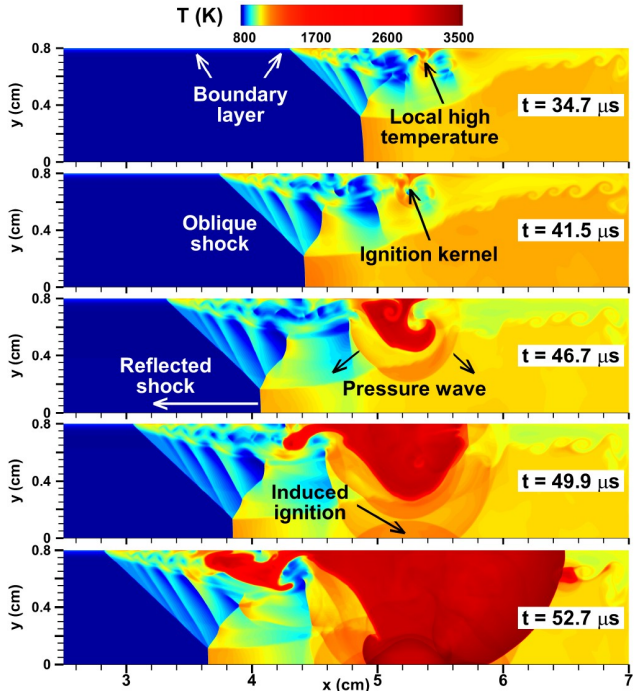

Figure 7 Evolution of temperature contour during the weak ignition process in a stoichiometric H_2/O_2 mixture with T_5 = 1068 K and P_5 = 2.8 atm.

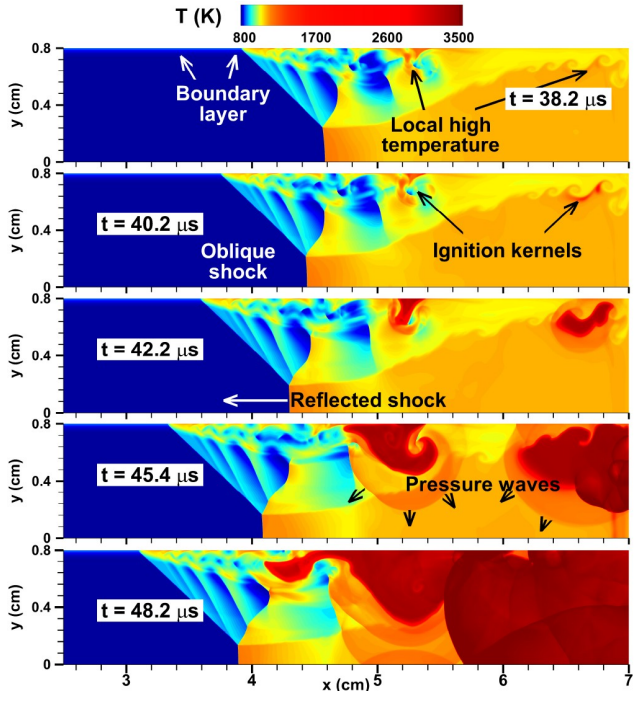

Figure 8 Evolution of temperature contour during the ignition process in a stoichiometric H_2/O_2 mixture with T_5 = 1073 K and P_5 = 2.8 atm.

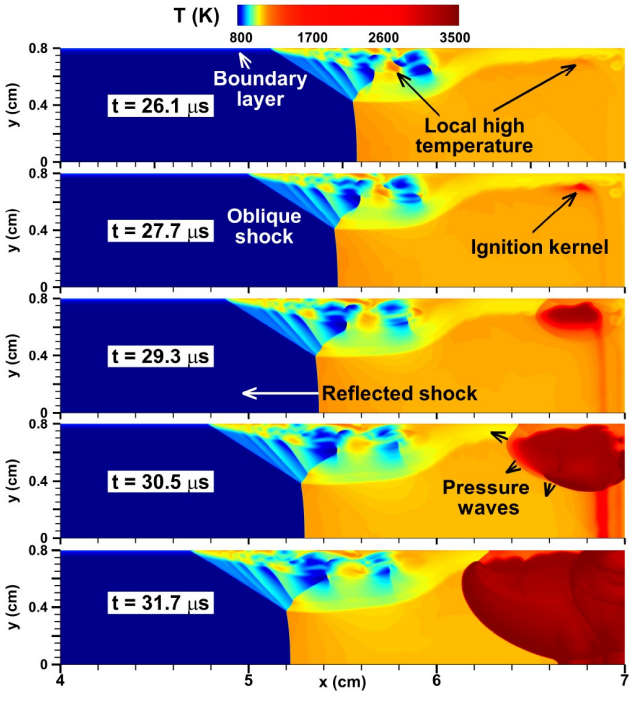

Figure 9 Evolution of temperature contour during the ignition process in a stoichiometric H_2/O_2 mixture with T_5 = 1091 K and P_5 = 2.8 atm.

mixture first compressed by the reflected shock. Though several hot spots with relatively high temperatures are formed at the foot of the bifurcated shock, its temperature is lower than that near the end wall. Consequently, the mixture closer to the corner ignites first. Meanwhile, the mixture close to the end wall and at the central region also ignites spontaneously due to its high reactivity. These two ignition regions merge with each other, resulting in the global ignition of the mixture behind the reflected shock. Similar phenomena were also observed by Knisely et al. [41] and Asahara et al. [27].

Finally, the post-reflected shock temperature is further increased to T_5 = 1146 K and Fig. 10 shows that the ignition first occurs near the end wall. A nearly planar ignition front quickly consumes the H_2/O_2 mixture compressed by the reflected shock. The ignition front propagates at a speed much higher than the reflected shock. Consequently, the reactant after the reflected shock can be considered to be consumed by a homogeneous ignition process.

Figures 7-10 indicate that with the increase of the post-reflected shock temperature, the ignition behavior gradually transits from the weak ignition at the foot of bifurcated shock to the strong ignition starting from the end wall.

Figure 11 compares the IDT recorded in 2D simulations with that predicted by 0D constant-volume homogeneous ignition. The results are also listed in Table 1. For strong ignition, a very good agreement between 2D and 0D results is achieved. However, at relatively low post-reflected shock temperature, weak ignition happens and the IDT from 2D simulations is much smaller than that from 0D simulations. This is because the local hot spot and ignition around the foot of the shock bifurcation accelerate the global ignition behind the reflected shock. Therefore, the occurrence of weak ignition has a great impact on the IDT measurement in shock tube experiments.

The sensitivity of IDT to the post-reflected shock temperature has been used in previous studies as a criterion to distinguish the weak ignition from the strong ignition. Based on experimental and numerical results for stoichiometric H_2/O_2 mixtures, Meyer and Oppenheim [26] proposed the critical value of $\partial\tau_{ig}/\partial T_5 = -2$ μs/K for the strong ignition limit. We also examine this ignition criterion through simulations and compare it with the results of other studies [6,26], which is shown in Fig. 12.

It is seen that the sensitivity criteria of Meyer and Oppenheim [26] well represents the boundary between weak and strong ignition for the stoichiometric H_2/O_2 mixture. Since ignition is more sensitive to temperature changes at larger absolute values of the sensitivity, $|\partial\tau_{ig}/\partial T_5|$, the local high-temperature kernels induced by the reflected shock and boundary interaction can easily trigger local weak ignition behind the reflected shock. Therefore, weak ignition occurs under relatively high sensitivity conditions as shown in Fig. 12. At a relatively high temperature, the sensitivity, $|\partial\tau_{ig}/\partial T_5|$, becomes small and thereby strong ignition is observed as shown in Fig. 12. It is noted that the boundary between weak and strong criterion collapses well, by coincidence, with the extension of the second explosion limit at relatively high pressures, while there is considerable deviation at relatively low pressures.

Though the sensitivity, $\partial\tau_{ig}/\partial T_5$, predicts the boundary between weak and strong ignition well, it does not take into account the IDT. With the increase of the IDT, the interaction

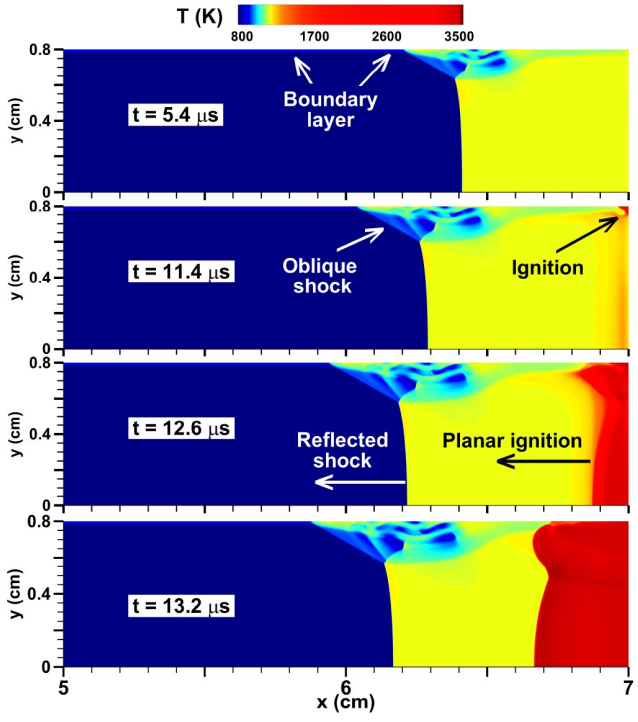

Figure 10 Evolution of temperature contour during the ignition process in a stoichiometric H_2/O_2 mixture with T_5 = 1146 K and P_5 = 2.8 atm.

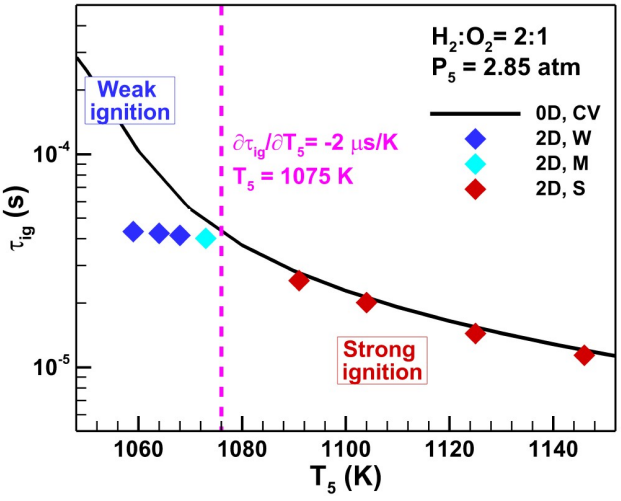

Figure 11 Comparison of ignition delay time from 2D simulations and 0D constant-volume (CV) homogeneous ignition for a stoichiometric H_2/O_2 mixture at P_5 = 2.85 atm. W and S represent weak and strong ignition, respectively, and M denotes the mixed mode of weak and strong ignition.

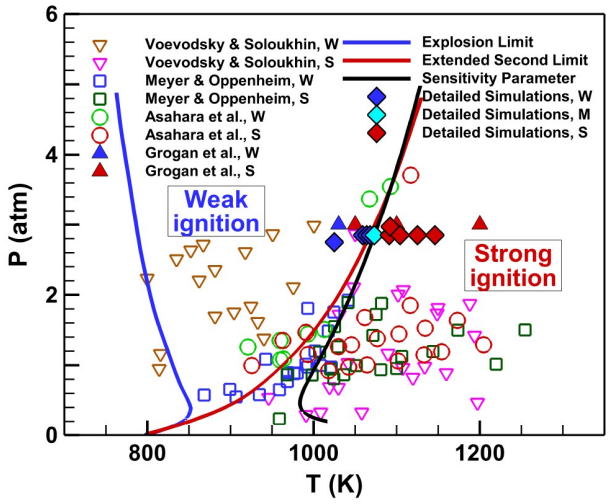

Figure 12 Explosion limit (blue line), extended second limit (red line) and the sensitivity parameter of $\partial\tau_{ig}/\partial T_5 = -2$ μs/K (black line) in the plot of pressure versus temperature for a stoichiometric H_2/O_2 mixture. The open symbols represent experimental results from the literature, and the closed symbols represent simulation results from Grogan and Ihme [6] (triangles) and this work (diamonds). W and S represent weak and strong ignition, respectively, and M denotes the mixed mode of weak and strong ignition.

between the reflected shock and boundary layer becomes longer and thereby the size of the bifurcated shock becomes larger, which results in more cold gas contamination and stronger mixing. This might prevent the formation of local high-temperature spots and thereby inhibit the local weak ignition. Consequently, a shorter IDT might be helpful for the appearance of weak ignition. To take into account this fact, we propose to use the relative sensitivity, $(\partial\tau_{ig}/\partial T_5)/\tau_{ig}$ or $\partial\ln\tau_{ig}/\partial T_5$, to characterize the condition for weak ignition. The increase of $\partial\tau_{ig}/\partial T_5$ and the decrease of τ_{ig} both help to induce the weak ignition.

Figure 13 shows the IDT, sensitivity and relative sensitivity of IDT to the post-reflected shock temperature for a stoichiometric H_2/O_2 mixture. The IDT and sensitivity both decrease exponentially with the temperature when the temperature is within a certain range. At low temperature, the relative sensitivity, $\partial\ln\tau_{ig}/\partial T_5$, reaches its peak value, and thereby the local high-temperature spots can readily induce weak ignition. Though the sensitivity, $\partial\tau_{ig}/\partial T_5$, can effectively distinguish the weak and strong for a stoichiometric H_2/O_2 mixture, the relative sensitivity, $\partial\ln\tau_{ig}/\partial T_5$, needs to be introduced for other fuels, especially for fuels with long IDT. It is noted that the sensitivity analysis of IDT can only qualitatively characterize the ignition mode behind the reflected shock.

3.3 Results for DME/O_2 mixtures

In this subsection, the ignition of the stoichiometric DME/O_2 mixture is considered. First, its IDT and its sensitivity and relative sensitivity are shown in Fig. 14. Since the logarithmic scale is used for the sensitivity, only the positive value of $(-\partial\tau_{ig}/\partial T_5)$ is shown. Figure 14 shows that the IDT changes non-monotonically with the temperature and the NTC behavior appears within a certain temperature range. Around the NTC region, the sensitivity, $-\partial\tau_{ig}/\partial T_0$, becomes negative or close to zero. Consequently, a small temperature rise due to shock bifurcation cannot induce local ignition. Besides, the relative sensitivity, $-\partial\ln\tau_{ig}/\partial T_0$, for DME/$O_2$ is much smaller than that for H_2/O_2. Therefore, it is more difficult to achieve weak ignition in the DME/O_2 mixture than in the H_2/O_2 mixture.

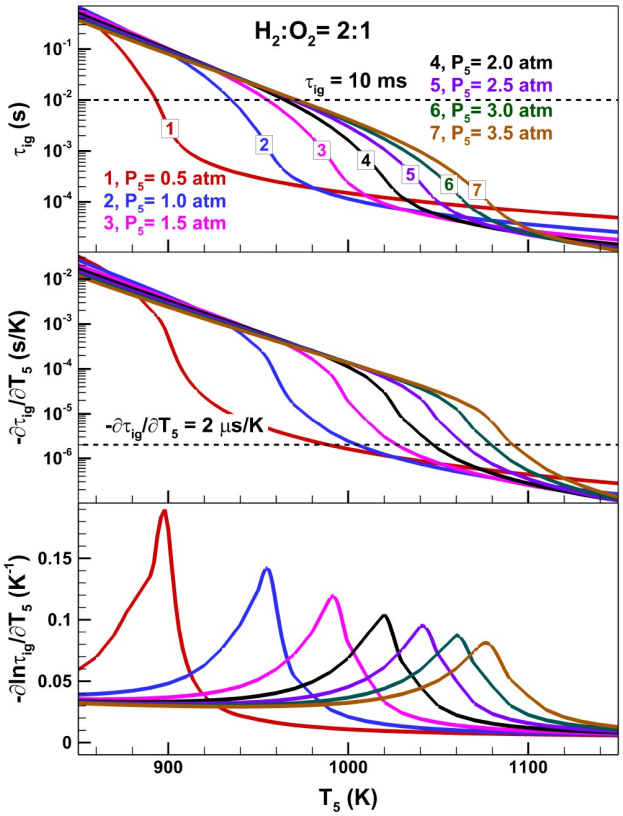

Figure 13 Change of the ignition delay time, the sensitivity and the relative sensitivity of ignition delay to the post-reflected shock temperature for a stoichiometric H_2/O_2 mixture at different pressures.

To show the validity of the above conclusion, we conduct 2D simulations considering detailed chemistry and transport for a stoichiometric DME/O_2 mixture under low post-shock temperature conditions. Three cases corresponding to the open circles in Fig. 14a are considered. The results for the case of $T_5 = 797$ K and $P_5 = 15$ atm are shown in Fig. 15. In Fig. 15a, several spots with local high temperatures are observed around the foot of the bifurcation at $t = 54.6$ μs. As discussed before, such local high temperature is caused by the strong viscous dissipation and pressure work during the reflected shock and boundary layer interaction. Since the IDT corresponding to the highest temperature in these hot spots is still relatively long, no local ignition is observed. The vortexes originating from the boundary layer detach and

move downstream carrying the mixture with relatively high temperature, which gradually dissipates in the main flow by strong mixing. This further prevents the local ignition in these hot spots.

On the other hand, compared with the mixture far away from the end wall, the mixture near the end wall is compressed earlier by the reflected shock. This makes the ignition first occur near the corner between the end wall and side wall around t = 311.4 μs as shown in Fig. 15b. This eventually induces strong ignition behind the reflected shock. For the other two cases with (T_5 = 895 K and P_5 = 15 atm) and (T_5 = 855 K and P_5 = 30 atm) marked in Fig. 14a, strong ignition is also observed. Therefore, compared to the H_2/O_2 mixture, it is much more difficult to achieve weak ignition in the DME/O_2 mixture.

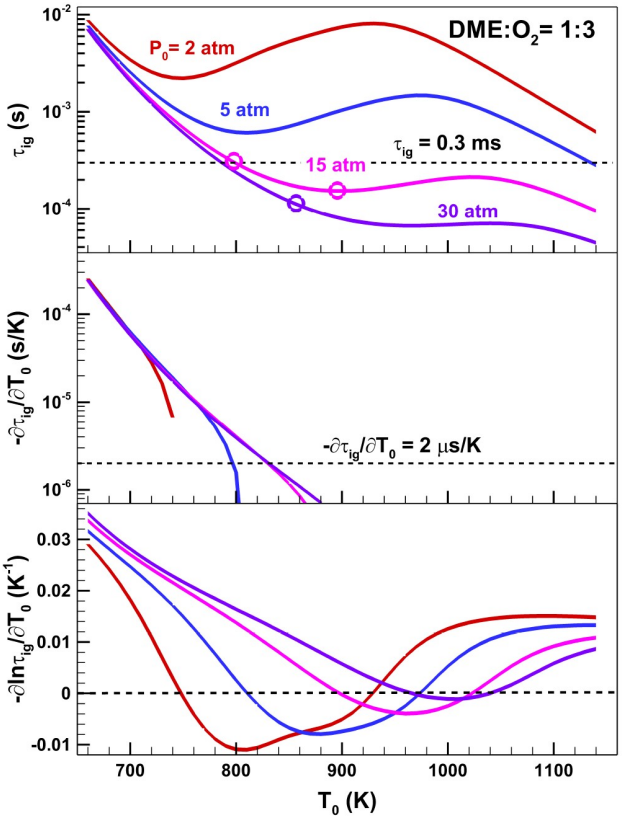

Figure 14 Change of the ignition delay time, the sensitivity and the relative sensitivity of ignition delay to the post-reflected shock temperature for a stoichiometric DME/O_2 mixture at different pressures.

4. Conclusions

2D transient simulations are conducted for shock bifurcation and local ignition induced by the interaction between the reflected shock and the boundary layer. Both stoichiometric H_2/O_2 and DME/O_2 mixtures are considered. Detailed chemistry and transport are included in simulations that use block-structured adaptive mesh refinement to efficiently resolve the reflected shock and the boundary layer interaction.

For the stoichiometric H_2/O_2 mixture considered in 2D simulations, the formation and evolution of shock bifurcation are analyzed. It is demonstrated that the viscous dissipation and pressure work are the main causes for local temperature rise around the bifurcated shock. The viscous dissipation dominates at the very beginning after the shock reflection,

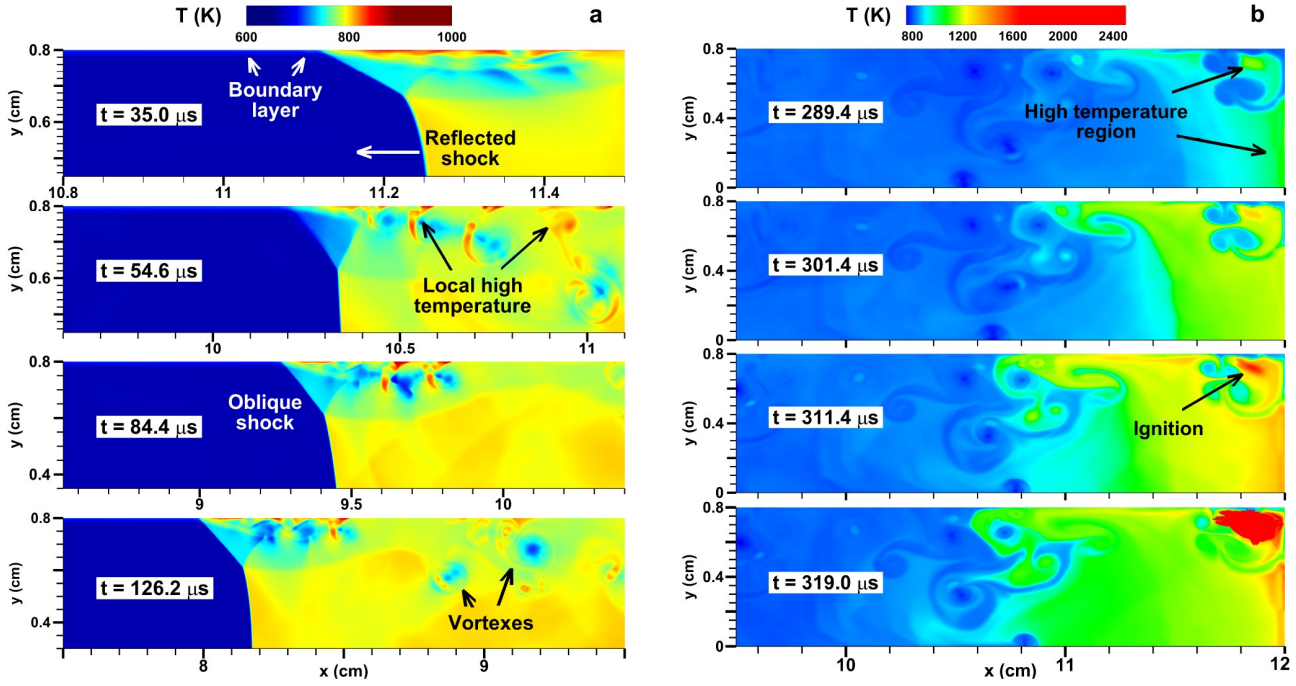

Figure 15 Evolution of temperature contour during the ignition process for a stoichiometric DME/O_2 mixture with T_5 = 797 K and P_5 = 15 atm: **a** reflected shock and boundary layer interaction, **b** strong ignition process.

while the pressure work gradually dominates during the subsequent evolution. It is found that local ignition happens at these hot spots, which results in non-uniform ignition after the reflected shock and weak ignition. With the increase of the post-reflected shock temperature, there is a gradual transition from weak ignition (occurring at the foot of bifurcated shock due to the reflected shock and boundary layer interaction) to strong ignition occurring near the end wall. A mixed-mode of weak and strong ignition is identified for the stoichiometric H_2/O_2 mixture.

Though the sensitivity, $\partial\tau_{ig}/\partial T_5$, can effectively distinguish the weak and strong for a stoichiometric H_2/O_2 mixture, the relative sensitivity, $\partial\ln\tau_{ig}/\partial T_5$, needs to be introduced for other fuels with long ignition delay time. Compared with the H_2/O_2 mixture, it is much more difficult to achieve weak ignition in the DME/O_2 mixture which has a relatively longer ignition delay time and smaller relative sensitivity.

It is noted that only 2D simulations are conducted here due to the computational cost limit. The 2D model considered here is not representative of the three-dimensional process in practical shock tube experiments. For example, viscous dissipation and vortex evolution are certainly affected by 3D effects. In future studies, it would be interesting to conduct 3D simulations for shock bifurcation and local ignition induced by the interaction between the reflected shock and the boundary layer.

This work was supported by the National Natural Science Foundation of China (Grant Nos. 52006001, and 52176096). We thank Prof. Shengkai Wang at Peking University, Dr. Song Chen at Technische Universität München and Dr. Wang Han at University of Edinburgh for helpful discussion.

1 N. A. Fomin, 110 years of experiments on shock tubes, J. Eng. Phys. Thermophy. **83**, 1118 (2010).
2 N. Chaumeix, B. Imbert, L. Catoire, and C. E. Paillard, The onset of detonation behind shock waves of moderate intensity in gas phase, Combust. Sci. Tech. **186**, 607 (2014).
3 R. K. Hanson, and D. F. Davidson, Recent advances in laser absorption and shock tube methods for studies of combustion chemistry, Prog. Energy Combust. Sci. **44**, 103 (2014).
4 G. A. Pang, D. F. Davidson, and R. K. Hanson, Experimental study and modeling of shock tube ignition delay times for hydrogen-oxygen-argon mixtures at low temperatures, Proc. Combust. Institut. **32**, 181 (2009).
5 E. L. Petersen, and R. K. Hanson, Nonideal effects behind reflected shock waves in a high-pressure shock tube, Shock Waves **10**, 405 (2001).
6 K. P. Grogan, and M. Ihme, Weak and strong ignition of hydrogen/oxygen mixtures in shock-tube systems, Proc. Combust. Institut. **35**, 2181 (2015).
7 J. T. Lipkowicz, I. Wlokas, and A. M. Kempf, Analysis of mild ignition in a shock tube using a highly resolved 3D-LES and high-order shock-capturing schemes, Shock Waves **29**, 511 (2019).
8 C. Huang, C. Qi, and Z. Chen, Non-uniform ignition behind a reflected shock and its influence on ignition delay measured in a shock tube, Shock Waves **29**, 957 (2019).
9 H. Yamashita, J. Kasahara, Y. Sugiyama, and A. Matsuo, Visualization study of ignition modes behind bifurcated-reflected shock waves, Combust. Flame **159**, 2954 (2012).
10 Y. Uygun, S. Ishihara, and H. Olivier, A high pressure ignition delay time study of 2-methylfuran and tetrahydrofuran in shock tubes, Combust. Flame **161**, 2519 (2014).
11 T. Javed, J. Badra, M. Jaasim, E. Es-Sebbar, M. F. Labastida, S. H. Chung, H. G. Im, and A. Farooq, Shock tube ignition delay data affected by localized ignition phenomena, Combust. Sci. Tech. **189**, 1138 (2016).
12 E. Ninnemann, B. Koroglu, O. Pryor, S. Barak, L. Nash, Z. Loparo, J. Sosa, K. Ahmed, and S. Vasu, New insights into the shock tube ignition of H_2/O_2 at low to moderate temperatures using high-speed end-wall imaging, Combust. Flame **187**, 11 (2018).
13 H. Mark, The interaction of a reflected shock wave with the boundary layer in a shock tube, NACA, TM-1418, (1958).
14 L. Davies, The Interaction of the Reflected Shock with the Boundary Layer in a Shock Tube and Its Influence on the Duration of Hot Flow in the Reflected-shock Tunnel, Part I, Dissertation for Doctoral Degree (1965).
15 L. Davies, and J. L. Wilson, Influence of reflected shock and boundary-layer interaction on shock-tube flows, Phys. Fluids **12**, I-37 (1969).
16 H. Kleine, V. Lyakhov, L. Gvozdeva, and H. Grönig, Bifurcation of a reflected shock wave in a shock tube, in: K. Takayama, ed. Shock Waves (Springer, Berlin, 1992) p. 261.
17 K. Matsuo, S. Kawagoe, and K. Kage, The interaction of a reflected shock wave with the boundary layer in a shock tube, Bull. JSME **17**, 1039 (1974).
18 Y. S. Weber, E. S. Oran, J. P. Boris, and J. D. Anderson Jr., The numerical simulation of shock bifurcation near the end wall of a shock tube, Phys. Fluids **7**, 2475 (1995).
19 V. Daru, and C. Tenaud, Evaluation of TVD high resolution schemes for unsteady viscous shocked flows, Comput. Fluids **30**, 89 (2000).
20 V. Daru, and C. Tenaud, Numerical simulation of the viscous shock tube problem by using a high resolution monotonicity-preserving scheme, Comput. Fluids **38**, 664 (2009).
21 K. P. Grogan, and M. Ihme, Regimes describing shock boundary layer interaction and ignition in shock tubes, Proc. Combust. Institut. **36**, 2927 (2017).
22 S. Chen, Q. Sun, I. Klioutchnikov, and H. Olivier, Numerical study of chemically reacting flow in a shock tube using a high-order point-implicit scheme, Comput. Fluids **184**, 107 (2019).
23 E. L. Petersen, and R. K. Hanson, Measurement of reflected-shock bifurcation over a wide range of gas composition and pressure, Shock Waves **15**, 333 (2006).
24 R. A. Strehlow, and A. Cohen, Limitations of the reflected shock technique for studying fast chemical reactions and its application to the observation of relaxation in nitrogen and oxygen, J. Chem. Phys. **30**, 257 (1959).
25 V. V. Voevodsky, and R. I. Soloukhin, On the mechanism and explosion limits of hydrogen-oxygen chain self-ignition in shock waves, Sym. (Int.) Combust. **10**, 279 (1965).
26 J. W. Meyer, and A. K. Oppenheim, On the shock-induced ignition of explosive gases, Sym. (Int.) Combust. **13**, 1153 (1971).
27 M. Asahara, Y. Shirakawa, A. Hayashi, and N. Tsuboi, Strong and mild ignition mechanism behind reflected shock waves in hydrogen mixture, in: 4th International Seminar on Fire and Explosion Hazards (2013).
28 R. Deiterding, Parallel Adaptive Simulation of Multi-dimensional Detonation Structures, Dissertation for Doctoral Degree (Brandenburg University of Technology, Senftenberg, 2003).
29 R. Deiterding, A parallel adaptive method for simulating shock-induced combustion with detailed chemical kinetics in complex domains, Comput. Struct. **87**, 769 (2009).
30 R. Deiterding, Block-structured adaptive mesh refinement-theory, implementation and application, ESAIM-Proc. **34**, 97 (2011).

31 R. Deiterding, High-resolution numerical simulation and analysis of Mach reflection structures in detonation waves in low-pressure H_2-O_2-Ar mixtures: A summary of results obtained with the adaptive mesh refinement framework AMROC, J. Combust. **2011**, 1 (2011).
32 J. L. Ziegler, Simulations of Compressible, Diffusive, Reactive Flows with Detailed Chemistry using a High-order Hybrid WENO-CD Scheme, Dissertation for Doctoral Degree (California Institute of Technology, Pasadena, 2012).
33 Y. Wang, C. Huang, R. Deiterding, H. Chen, and Z. Chen, Propagation of gaseous detonation across inert layers, Proc. Combust. Institut. **38**, 3555 (2021).
34 Y. Wang, Z. Chen, and H. Chen, Diffraction of weakly unstable detonation through an obstacle with different sizes and shapes, Phys. Rev. Fluids **6**, 043201 (2021).
35 J. Li, Z. Zhao, A. Kazakov, and F. L. Dryer, An updated comprehensive kinetic model of hydrogen combustion, Int. J. Chem. Kinet. **36**, 566 (2004).
36 A. Bhagatwala, Z. Luo, H. Shen, J. A. Sutton, T. Lu, and J. H. Chen, Numerical and experimental investigation of turbulent DME jet flames, Proc. Combust. Institut. **35**, 1157 (2015).
37 C. Huang, Numerical Studies on Shock-induced Ignition and Detonation Development, Dissertation for Doctoral Degree (Peking University, Beijing, 2020).
38 J. Damazo, J. Ziegler, J. Karnesky, and J. E. Shepherd, Investigating shock wave-boundary layer interaction caused by reacting detonations, in: 8th International Symposium on Hazards, Prevention and Mitigation of Industrial Explosions (Yokohama, 2010).
39 A. Deshpande, and B. Puranik, Effect of viscosity and wall heat conduction on shock attenuation in narrow channels, Shock Waves **26**, 465 (2016).
40 G. Wilson, S. Sharma, and W. Gillespie, Time-dependent simulation of reflected-shock/boundary layer interaction, in: 31st Aerospace Sciences Meeting (Reno, 1993).
41 A. Knisely, J. M. Austin, C. Bacon, and A. Khokhlov, Strong and weak ignition in $2H_2 + O_2$ behind reflected shocks in two-dimensional Navier-Stokes simulations with detailed chemistry, in: 29th International Symposium on Shock Waves (Springer, Berlin, 2013).
42 J. H. Lee, R. Knystautas, and N. Yoshikawa, Photochemical initiation of gaseous detonations, Acta Astronaut. **5**, 971 (1978).
43 R. Blumenthal, K. Fieweger, K. H. Komp, and G. Adomeit, Gas dynamic features of self ignition of non diluted fuel/air mixtures at high pressure, Combust. Sci. Tech. **123**, 1 (1997).

反射激波与边界层相互作用引起弱点火和强点火的数值研究

黄成扬, 王　元, DeiterdingRalf, 于德海, 陈　正

摘要　在激波管实验中, 反射激波与边界层的相互作用会导致激波分叉和弱点火. 在激波管实验中, 弱点火会严重影响点火延迟时间的测量. 在考虑详细的化学和输运效应下, 本文通过二维数值模拟研究反射激波后的激波分岔和非均匀点火, 以解释反射激波和边界层相互作用引发激波分岔的形成机理, 并研究氢和二甲醚的弱点火及其向强点火的转变. 研究发现入射激波在端壁的非均匀反射会在壁面产生一个楔形斜激波脚. 楔形结构导致反射激波和边界层之间的强烈相互作用, 从而导致激波分岔. 结果表明分叉激波底部的局部高温点产生于黏性耗散和压力功. 随着反射后激波温度的升高, 在化学计量氢/氧混合物中观察到从弱点火到强点火的转变. 通过引入点火延迟时间对反射后激波温度的相对灵敏度, 可以表征反射激波后弱点火出现. 与氢/氧混合物不同, 在二甲醚/氧混合物中未观察到弱点火现象, 因为其具有相对较长的点火延迟时间和较小的相对灵敏度.